Published by Avanti Publishers

Journal of Chemical Engineering Research Updates

ISSN (online): 2409-983X

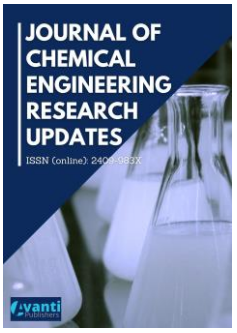

Photocatalytic Reduction of Cr(VI) and Degradation of Organic Pollutants by Z-Scheme g-C_3N_4/Bi_2S_3 Heterojunction

Lin Ding*, Ying Deng, Xinggang Liu, Lingling Liu, Jingjing Ding and Fang Deng

National-Local Joint Engineering Research Center of Heavy Metal Pollutants Control and Resource utilization, Nanchang Hangkong University, Nanchang 330063, PR China

ARTICLE INFO

Article Type: Research Article

Keywords:
g-C3N4/Bi2S3
Photocatalysis
Cr(VI) reduction
Organic pollutant
Z-scheme heterojunction

Timeline:
Received: December 12, 2021
Accepted: February 15, 2022
Published: March 22, 2022

Citation: Ding L, Deng Y, Liu X, Liu L, Ding J, Deng F. Photocatalytic Reduction of Cr(VI) and Degradation of Organic Pollutants by Z-Scheme g-C_3N_4/Bi_2S_3 Heterojunction. J Chem Eng Res Updates, 2022; 9: 1-12.

DOI: https://doi.org/10.15377/2409-983X.2022.09.1

ABSTRACT

Photocatalytic reduction of hexavalent Cr(VI) couping oxidative degradation of organic contamination is an emerging and practical approach for water treatment. In this study, Z-scheme g-C_3N_4/Bi_2S_3 heterojunctions with intimate interface were successfully synthesized by direct growth of Bi_2S_3 on g-C_3N_4 surface. Notably, the photocatalytic performance of Z-scheme g-C_3N_4/Bi_2S_3 was influenced by g-C_3N_4 content. The optimized 2% g-C_3N_4/Bi_2S_3 heterojunction shows the highest photocatalytic reduction performance with 93.4% reduction efficiency of Cr(VI) under UV-visible light due to efficient separation and transfer of charge carriers and proper band structure. Furthermore, 2% g-C_3N_4/Bi_2S_3 can degrade tetracycline and Rhodamine B. Free radical capturing and quantitative tests indicate that holes and superoxide radicals are primary active species for the degradation of organic pollutants, while Cr(VI) was reduced to Cr(III) by the photogenerated electrons. Overall, this study provides new insight into the synthesis of high-performance Z-scheme heterojunctions for the future advancement of photocatalysis technology.

*Corresponding Author
Email: dinglin_hust@126.com
Tel: +86 7913953373

1. Introduction

In the light of increasing industrialization and urbanization, water pollution by heavy metal and organic pollutants has been a global problem, which threatens the entire biosphere and impacts the lives of people worldwide [1, 2]. Chromium (Cr) is mainly discharged from tanneries, printing, pigments, and metal plating, which is considered to be carcinogenic and mutagenic to living organisms [3, 4]. Generally, chromium in aquatic ecosystems exists as Cr(III) and Cr(VI) [5]. Hexavalent Cr(VI) has a much higher toxicity than trivalent Cr(III), while Cr(III) can be naturally formed in the earth's crust and is one of the essential trace elements for humans indeed [6]. Therefore, the conversion of chromium from the highly toxic Cr(VI) into low toxic or non-toxic valence is considered an effective strategy to mitigate the potential hazards of chromium pollutants.

Photocatalysis is regarded as one of the most promising technologies due to its high efficiency, eco-friendliness, utilizing solar energy, mild reaction conditions, and low energy consumption [7, 8]. It has broad application prospects in the remedy of environmental pollution. The photogenerated electrons can transform highly toxic Cr(VI) anions into Cr(III), and some reactive species produced in the photocatalytic process can destroy the structure of organic pollutants, leading to their degradation [9]. Different types of semiconductor photocatalysts, including TiO_2 [10, 11], CdS [12], CeO_2 [13], and $BiVO_4$ [14], have been fabricated for the remedy of environmental pollution. However, it is difficult for a single-component catalyst to have both a wide light absorption range and strong redox ability, and photogenerated electrons and holes can recombine each other easily [15].

One class of the leading photocatalysts that could answer these challenges is hetero-nanostructured semiconductors. These photocatalysts are compelling choices for photocatalytic reduction of hexavalent Cr(VI). It is attributed to their synergies by assimilating favorable characteristics and conquering the incapability of pure semiconductors to widen light absorption range, promote the separation of photogenerated electron-hole pairs, and optimize redox ability [16, 17]. As a promising semiconductor, bismuth sulfide (Bi_2S_3) has attracted widespread attention due to its advantages of remarkable photoconductivity, low cost, and nontoxicity [18, 19]. Despite their bright features, pure Bi_2S_3 has rarely been used for practical application because of the rapid recombination of photogenerated charge carriers [20]. Hence, the combination of Bi_2S_3 with other proper semiconductors for constructing Z-scheme heterojunctions is necessary to enhance photocatalytic performance. Graphitic carbon nitride (g-C_3N_4) with π-conjugated inorganic polymer construction has remarkable photoconductivity and a wide bandgap (2.7~5.49 eV), and it still suffers from insufficient utilization of visible light and fast recombination of photogenerated electrons and holes [21-23]. Thus, the construction of Z-scheme g-C_3N_4/Bi_2S_3 heterojunctions is expected to overcome the above shortcomings.

In this work, Z-scheme g-C_3N_4/Bi_2S_3 heterojunction with intimate contact interface was fabricated using in-situ growth technology. Its photocatalytic activity was evaluated by Cr(VI) reduction and degradation of tetracycline and Rhodamine B. Furthermore, enhancement of performance and photocatalytic mechanism of g-C_3N_4/Bi_2S_3 were systematically discussed. Z-scheme g-C_3N_4/Bi_2S_3 heterojunction exhibited superior photocatalytic performance compared with pure g-C_3N_4 and Bi_2S_3. Besides, the content of g-C_3N_4 dramatically influences the photocatalytic activity of g-C_3N_4/Bi_2S_3 heterojunctions. The present study will pave the way for further developing high-efficient Z-scheme heterojunctions to simultaneously reduce the toxicity of heavy metal anion and organic contaminants.

2. Experimental

2.1. Reagents

Potassium dichromate ($K_2Cr_2O_7$), bismuth nitrate pentahydrate ($Bi(NO_3)_3$•$5H_2O$), melamine ($C_3N_3(NH_2)_3$), thioacetamide (CH_3CSNH_2), diphenylcarbazide ($C_{13}H_{14}N_4O$), ethylene glycol (EG), and isopropanol (IPA) were purchased from Xilong Chemical Co., Ltd.). Triethanolamine (TEOA) and p-benzoquinone (BQ) were obtained from Shanghai Chemical Reagent Co., Ltd. and Shanghai Jingchun Reagent Co., Ltd., respectively. All materials are of analytical grade.

2.2. Synthesis of g-C_3N_4

The detailed operation process for the synthesis of g-C_3N_4 is as follows [24-26]: 2.5 g $C_3N_3(NH_2)_3$ was added into two clean and dry alumina crucibles of the same size and calcined at 520 ℃ for 2 h with a heating rate of 5 ℃·min^{-1}. In order to fully deaminate to obtain pure g-C_3N_4, it is still necessary to keep it at 520 ℃ for another 2 h. After the reaction, the products were cooled to room temperature and ground in an agate mortar to get fine powder for later use.

2.3. Preparation of g-C_3N_4/Bi_2S_3 Composite Photocatalyst

(1) 5.84 g of $Bi(NO_3)_3·5H_2O$ was added to 50 mL of deionized water and stirred to disperse completely. Then, 3.76 g of thioacetamide (TAA) was slowly added to the mixtures with stirring for about 30 min;

(2) In the case of continuous stirring at room temperature, different amount of g-C_3N_4 was added and kept stirring for 30 min. Mixtures were poured into the reaction kettle and put in an oven at 180 ℃ for 12. After the hydrothermal reaction was over, the reaction system was cooled to room temperature. Then the precipitate was washed with deionized water and ethanol and dried at 60 ℃ for 12 h. The g-C_3N_4/Bi_2S_3 with different mass percent of C_3N_4 (x=0, 1%, 2%, and 5%) were obtained.

2.4. Evaluation of Photocatalytic Activity

2.4.1. Preparation of Chromogenic Agent

0.1 g of diphenylcarbohydrazide was added into 5 mL of acetone and was dissolved completely under ultrasonic conditions. Then mixture solution was diluted to 10 mL and stored at refrigeration temperature.

2.4.2. Batch Photocatalytic Reaction

The photocatalytic activity of g-C_3N_4/Bi_2S_3 was tested by reduction of Cr(VI) solution. Herein, 30 mg g-C_3N_4/Bi_2S_3 nanocomposites were suspended in 100 mL of 10 mg/L Cr(VI) solution. Then, the reaction solution was stirred in the dark for 40 min, and 3 mL samples were taken out every 20 min for the adsorption equilibrium of Cr(VI) on catalysts. After that, the reaction solution was immediately transferred to a xenon lamp simulating sunlight for irradiation, and magnetic stirring was kept. 3 ml of solution was taken out every 20 min and was filtered using 0.45 μm water system filter head for separating the catalysts. 0.5 mL of Cr(VI) sample, 50 μL chromogenic agent, and 1 mLof 2 mol/L H_2SO_4 were mixed well, then diluted to 5 mL with H_2O, and finally, the mixture was analyzed by a UV-vis spectrophotometer at 540 nm. The removal efficiency can be obtained according to the following equation:

$$\text{Removal efficiency } (\%) = \left(1 - \frac{C_t}{C_0}\right) \times 100\%$$

where C_t is the concentration of Cr(VI) at t min (mg/L), C_0 is the concentration of original Cr(VI) stock solution (mg/L).

2.5. Photocurrent and Mott-Schottky Test

2.5.1. Preparation of Working Electrode

Five glassy carbon electrodes with the same size and thickness, which ultrasonically cleaned with an appropriate amount of ethanol solution for 30 min, were placed in sequence on a tray padded with clean paper, and then the multimeter was adjusted to the ohm range to find the conductive surface of each glassy carbon electrode. 10 mg of the synthesized materials g-C_3N_4, Bi_2S_3, 1% g-C_3N_4/Bi_2S_3, 2% g-C_3N_4/Bi_2S_3, and 5%g-C_3N_4/Bi_2S_3 were dispersed in 50 mL ethanol solution and was coated on the bottom of the conductive surface of the glassy carbon electrode with an area of about 1 × 1 cm^2. It was then was dried in a ventilated place for 8 h.

2.5.2. Test

Photocurrent and Mott-Schottky tests are used to reflect the separation ability and flat band potential of photogenerated electron holes in materials under illumination. The Pt electrode was used as the anode, and Ag/AgCl electrode was generally used as the reference electrode. The working electrode was prepared in 2.5.1 to form a standard three-electrode system. The electrolytes here are 0.5 mol/L Na_2SO_4 solutions.

2.6. Characterization

The crystal structure of g-C_3N_4/Bi_2S_3 was determined using X-ray diffraction (XRD) (D8ADVANCE-A25, Bruker, Germany) with Cu-Kα radiation (λ=0.154056 nm). An AXIS Supra X-ray photoelectron spectrometry (Shimadzu, Japan) was employed to analyze the chemical state of elements and rectify the binding energies of g-C_3N_4/Bi_2S_3. UV-Vis diffuse reflectance spectroscopy (DRS) of g-C_3N_4/Bi_2S_3 was measured by U-3900H UV-Vis spectrophotometer (Hitachi, Japan) using $BaSO_4$ as a reference. The Brunauer-Emmett-Teller (BET) specific surface area and pore-size distribution of g-C_3N_4/Bi_2S_3 were measured using a GEMINI VII 2390 surface area and porosity analyzer (Micromeritics, USA). The photoluminescence (PL) spectra of g-C_3N_4/Bi_2S_3 samples were measured by an F-7000 Fluorescence spectrophotometer (HACH, USA).

2.7. Total Organic Carbon (TOC) and Chemical Oxygen Demand (COD) Removal of Actual Pharmaceutical Wastewater

2% g-C_3N_4/Bi_2S_3 was added in actual pharmaceutical wastewater, and the photocatalytic reaction condition is similar to the above. The samples were taken out every 1 h to explore the removal efficiency of TOC and COD.

3. Results and Discussion

3.1. X-ray Diffraction (XRD) and X-ray Photoelectron Spectroscopy (XPS)

Fig. (**1**) shows the XRD patterns of 2% g-C_3N_4/Bi_2S_3. The characteristic diffraction peaks of 2% g-C_3N_4/Bi_2S_3 at 2θ of 25.003°, 28.641°, 31.812°, 45.533°, 46.468°, and 52.753° can correspond to the (111), (121), (122), (200), (143) and (231) crystal planes of rhombic Bi_2S_3 (JCPDS No.84-0279). However, the characteristic diffraction peak of g-C_3N_4 was not observed in the 2% g-C_3N_4 /Bi_2S_3 heterojunction. The possible reason for this phenomenon is that the intensity of the diffraction peak is very low due to the low content of g-C_3N_4 in the composite material, which can be interfered with the diffraction peak of Bi_2S_3.

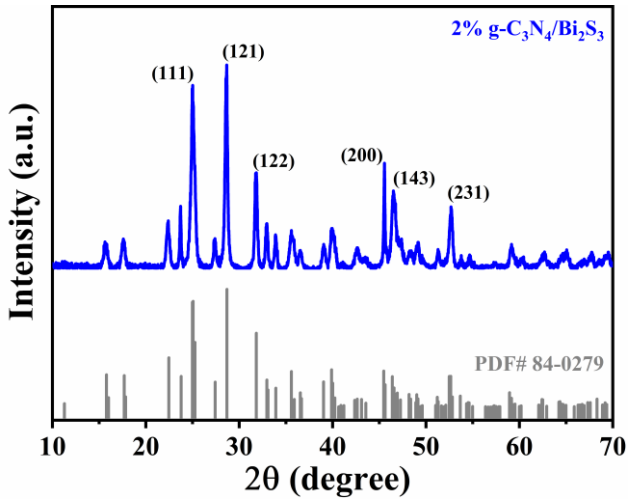

Figure 1: XRD patterns of 2% g-C_3N_4/Bi_2S_3.

XPS technology was used to analyze the elemental composition and chemical valence state of composite 2% g-C_3N_4/Bi_2S_3 (Fig. **2**). From Fig. **2**(a), we can see the appearance of elements Bi, S, C, and N, respectively, and the

corresponding binding energies of the Bi $4f_{5/2}$ and Bi $4f_{7/2}$ are 161.8 eV and 156.5 eV, respectively [19]. The S 2s peak is located at a binding energy of 223.5 eV. The peak of N 1s is located at the binding energy of 397.6 eV. The two C 1s peaks with binding energies of 286.8 eV and 282.9 eV were observed [27].

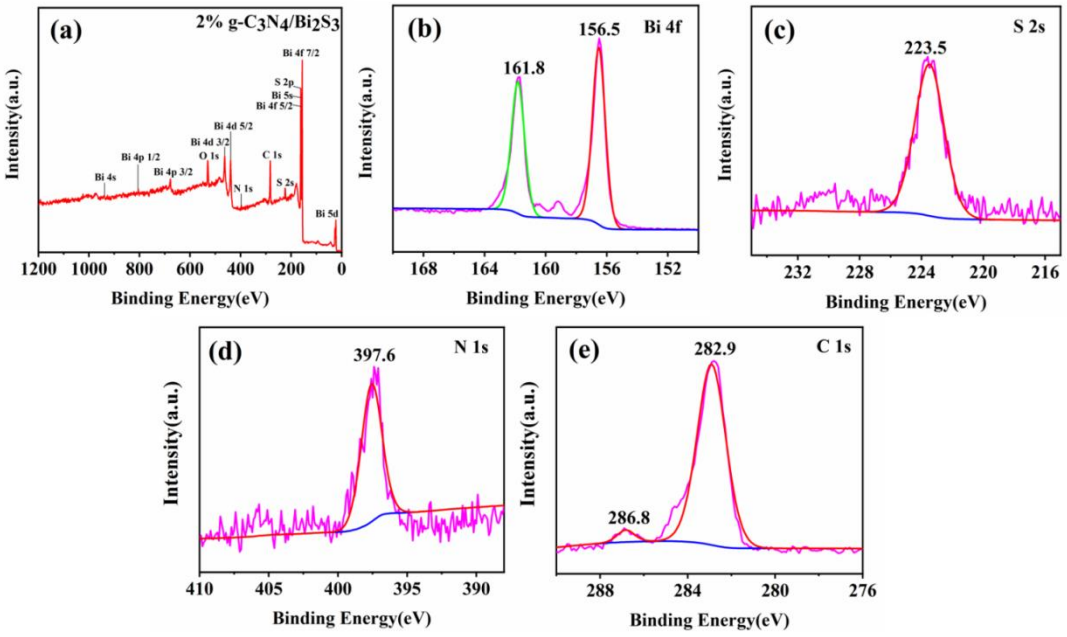

Figure 2: XPS spectrum of 2% g-C_3N_4/Bi_2S_3, (a) full element scan, (b) Bi 4f, (c) S 2s, (d) N 1s, (e) C 1s XPS pattern.

3.2. Specific Surface Area and Pore Structure (BET)

The specific surface area and pore size of the material can influence the adsorption performance of the catalysts. The N_2 adsorption-desorption isotherms of g-C_3N_4, Bi_2S_3, and 2% g-C_3N_4/Bi_2S_3 are shown in Fig. (**3**). The adsorption isotherms of g-C_3N_4, Bi_2S_3, and 2% g-C_3N_4/Bi_2S_3 belong to type IV adsorption isotherms, and pore size distribution is mainly in the range of 2 ~ 50 nm, indicating the mesoporous structure [5]. There is no central saturated adsorption platform on the adsorption isotherm, so it can be judged that they can be classified to the H3 hysteresis loop.

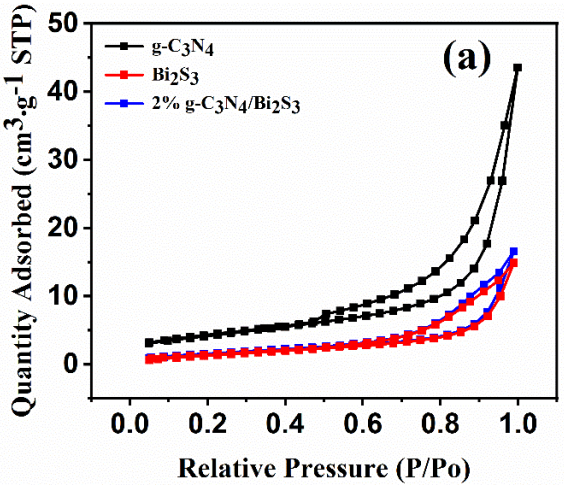

Figure 3: N_2 adsorption-desorption isotherm of g-C_3N_4, Bi_2S_3, and 2% g-C_3N_4/Bi_2S_3.

The parameters of specific surface area, pore-volume, and pore diameter of the three materials are listed in Table **1**. The specific surface areas of g-C_3N_4, Bi_2S_3, 2% g-C_3N_4/Bi_2S_3 are 15.07, 6.20, and 5.70 $m^2 \cdot g^{-1}$, respectively. Their pore volume is 0.067, 0.026 and 0.023 $cm^3 \cdot g^{-1}$, respectively. The pore size distribution is 13.45, 11.62, and

10.65 nm, respectively. The pore diameter, specific surface area, and pore volume of 2% g-C_3N_4/Bi_2S_3 are smaller than the pure material. These three indexes are not the only factors determining the photocatalytic performance of the material but also impact the sequent photocatalytic process.

Table 1: Specific surface area, pore-volume, and pore diameter of g-C_3N_4, Bi_2S_3, 2% g-C_3N_4/Bi_2S_3.

Samples	BET ($m^2 g^{-1}$)	Pore Volume ($cm^3 g^{-1}$)	Average Pore Size (nm)
g-C_3N_4	15.07	0.067	13.45
Bi_2S_3	6.20	0.026	11.62
2% g-C_3N_4/Bi_2S_3	5.70	0.023	10.65

3.3. Ultraviolet-Visible Diffuse Reflectance Spectroscopy (DRS)

The optical properties of g-C_3N_4, Bi_2S_3, and 2% g-C_3N_4/Bi_2S_3 were investigated by UV-Vis diffuse reflectance spectrometer. It can be seen from Fig. **4**(a) that the g-C_3N_4, Bi_2S_3, and 2% g-C_3N_4/Bi_2S_3 samples both have absorption in the visible light range (400 ~ 760 nm). The absorption intensity of 2% g-C_3N_4/Bi_2S_3 is higher than pure g-C_3N_4. After 760 nm, the absorption intensity of pure Bi_2S_3 is significantly reduced, but 2% g-C_3N_4/Bi_2S_3 still has a certain absorption strength and is higher than that of both two pure materials. It shows that 2% g-C_3N_4/Bi_2S_3 widens its absorption range in the solar spectrum and enhances its photocatalytic performance. The bandgap width can be obtained by the following formula:

$$(\alpha h\nu)^{\mathrm{n}} = \mathrm{k}\left(h\nu - \mathrm{E_g}\right)$$

Where *α*, *h*, and *v* are the light absorption coefficient, Planck's constant, and the frequency of light, respectively. k is the constant associated with the band tail [28].

Fig. **4**(b) shows $(\alpha h\nu)^2$ versus $h\nu$ curves. The band gap energy of g-C_3N_4, Bi_2S_3 and 2% g-C_3N_4/Bi_2S_3 are 1.817, 1.837 and 1.927 eV, respectively [29].

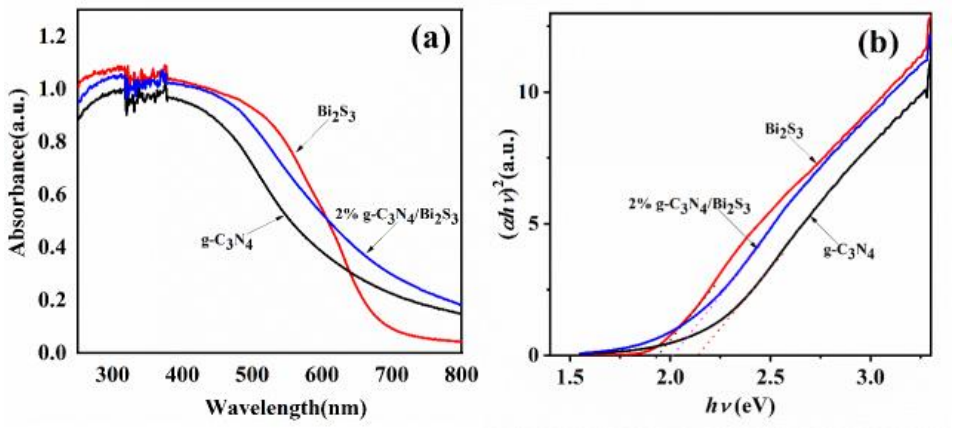

Figure 4: Ultraviolet-visible diffuse reflectance spectra of pure g-C_3N_4, Bi_2S_3, 2% g-C_3N_4/Bi_2S_3.

3.4. Fluorescence Spectrum Analysis (PL)

These PL spectra explore the photogenerated electron-hole recombination of g-C_3N_4, Bi_2S_3, and 2% g-C_3N_4/Bi_2S_3. Generally, lower fluorescence emission intensity means less photogenerated electron-hole recombination ability. As shown in Fig. (**5**), the fluorescence intensity is pure g-C_3N_4 > pure Bi_2S_3 > 2% g-C_3N_4/Bi_2S_3. The fluorescence intensity of the 2% g-C_3N_4/Bi_2S_3 composite is the smallest, indicating that electrons and holes can be separated quickly.

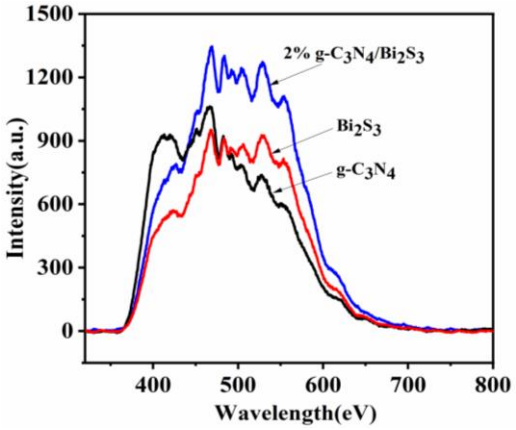

Figure 5: PL spectra of pure g-C_3N_4, Bi_2S_3 and 2% g-C_3N_4/Bi_2S_3.

3.5. Photocurrent and Mott-Schottky Analysis

Under visible light, the current response trend of photocatalytic materials can reflect the separation efficiency of photogenerated electrons and holes. The photocurrent responses of pure g-C_3N_4, Bi_2S_3, and 2% g-C_3N_4/Bi_2S_3 are systematically explored. It can be seen from Fig. **6** that the photocurrent increases as follows: pure g-C_3N_4 < Bi_2S_3 < 2% g-C_3N_4/Bi_2S_3, of which the photocurrent of 2% g-C_3N_4/Bi_2S_3 is about 3.1×10^{-8} μA and significantly higher than that of pure g-C_3N_4 and Bi_2S_3. It shows that the combination of pure g-C_3N_4 and Bi_2S_3 dramatically improves the separation rate of photogenerated electrons and holes, thus improving the photocatalytic redox performance of g-C_3N_4/Bi_2S_3 composites.

Consistent with the experimental environment of the photocurrent test, Mott-Schottky curves of g-C_3N_4, Bi_2S_3, and 2% g-C_3N_4/Bi_2S_3 were also obtained to explore the types of semiconductors and flat band potential (Fig. **7**). The slope of these curves is positive, indicating n-type semiconductors of g-C_3N_4, Bi_2S_3, and 2% g-C_3N_4/Bi_2S_3. The intersection of the slope and abscissa corresponds to the flat band potential (E_{FB}). As listed in Table **2**, the flat band potentials of pure g-C_3N_4, Bi_2S_3, and 2% g-C_3N_4/Bi_2S_3 are -0.55, -0.26, and -0.37 eV, respectively.

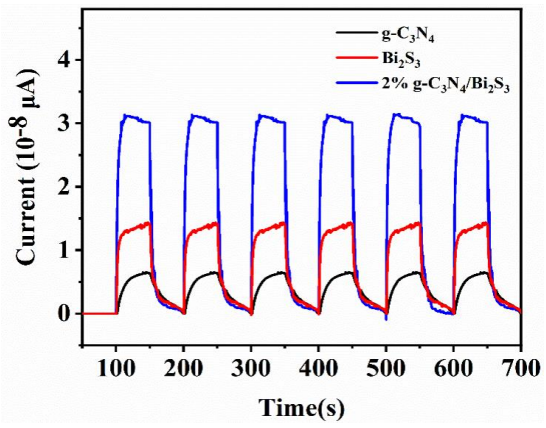

Figure 6: Photocurrent response of pure g-C_3N_4, Bi_2S_3, and 2% g-C_3N_4/Bi_2S_3.

Table 2: E_g, E_{FB}, E_{CB} and E_{VB} values of g-C_3N_4, Bi_2S_3 and 2% g-C_3N_4/Bi_2S_3.

Samples	E_g (eV)	E_{FB} (eV vs.Ag/AgCl)	E_{CB}≈E_{FB} (eV vs.NHE)	E_{VB} (eV)
g-C_3N_4	2.17	-0.55	-0.353	1.817
Bi_2S_3	1.9	-0.26	-0.063	1.837
2% g-C_3N_4/Bi_2S_3	2.1	-0.37	-0.173	1.927

Calculation basis: $E_{CB} = E_{FB} + 0.197$ (0.197 is the potential of the reference electrode Ag/AgCl electrode), $E_{VB} = E_g + E_{CB}$

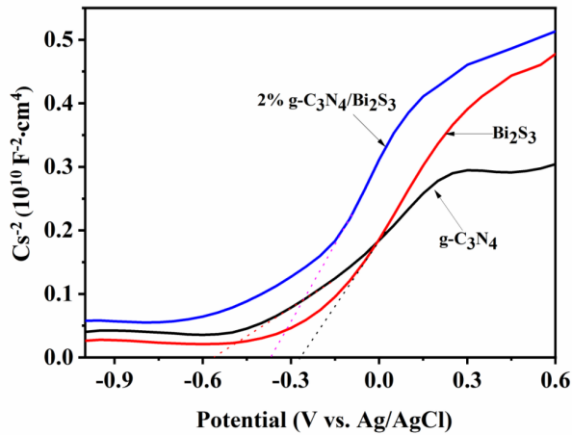

Figure 7: Mott-Schottky curves of pure g-C_3N_4, Bi_2S_3 and 2% g-C_3N_4/Bi_2S_3.

3.6. Evaluation of Photocatalytic Activity

The photocatalytic activity of pure g-C_3N_4, Bi_2S_3, and g-C_3N_4/Bi_2S_3 for reduction of Cr(VI) was measured under visible light and ultraviolet-visible light. As shown in Fig. **8**(a), under visible light conditions, the Cr(VI) reduction efficiencies of g-C_3N_4, Bi_2S_3, 1% g-C_3N_4/Bi_2S_3, 2% g-C_3N_4/Bi_2S_3 and 5% g-C_3N_4/Bi_2S_3 are 39.2%, 42.9%, 60.3%, 67.1% and 49.9%, respectively. The catalytic reduction efficiency of 2% g-C_3N_4/Bi_2S_3 is the highest, up to 67.1%.

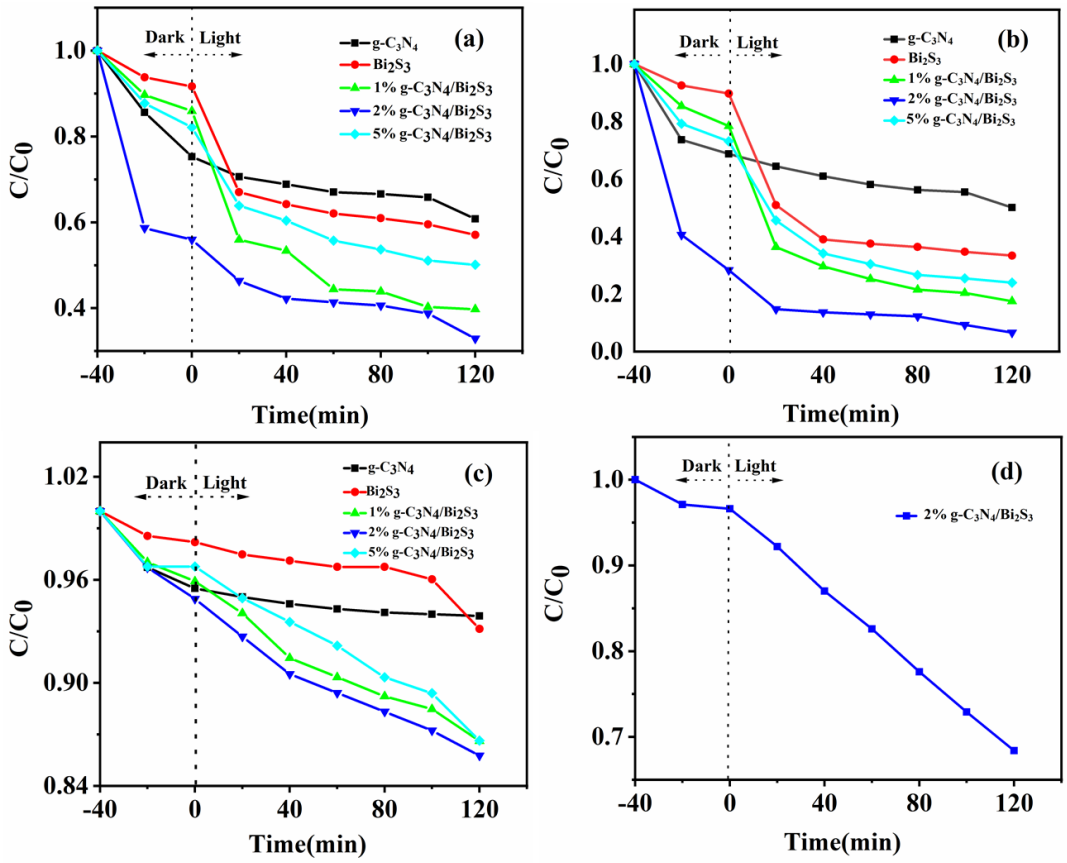

Figure 8: Photocatalytic efficiency of g-C_3N_4, Bi_2S_3 and 2% g-C_3N_4/Bi_2S_3: Reduction of Cr(VI) under visible light (a) and ultraviolet-visible light (b). Degradation of tetracycline (c) and Rhodamine B (d) under visible light.

As shown in Fig. **8**(b), under UV visible light conditions, the Cr(VI) reduction efficiencies by g-C_3N_4, Bi_2S_3, 1% g-C_3N_4/Bi_2S_3, 2% g-C_3N_4/Bi_2S_3 and 5% g-C_3N_4/Bi_2S_3 are 49.9%, 66.6%, 82.5%, 93.4% and 76.0%, respectively. Among

them, the photocatalytic reduction efficiency of Cr(VI) by 2% g-C_3N_4/Bi_2S_3 is the best. After 120 min, the catalytic reduction efficiency of Cr(VI) can reach 93.4%. The results demonstrate that an appropriate amount of g-C_3N_4 into Bi_2S_3 is beneficial for separating and migrating photogenerated electrons and holes. However, an excess of g-C_3N_4 is detrimental to the photocatalytic efficiency of g-C_3N_4/Bi_2S_3 due to the recombination of holes and electrons.

The degradation of tetracycline and Rhodamine B by 2% g-C_3N_4/Bi_2S_3 is present in Fig. **8**(c) and (d). It can be seen that 2% g-C_3N_4/Bi_2S_3 can degrade tetracycline (14.24%) and Rhodamine B (31.6%).

3.7. Activity Capture Experiment

To reveal the vital active species in the degradation of organic matter by 2% g-C_3N_4/Bi_2S_3, triethanolamine (TEOA), isophthalic acid (IPA), and p-benzoquinone (BQ) are selected as capturing agents to explore their effects on the degradation performance of Rhodamine B. TEOA is the capture agent of h^+, IPA is the capture agent of ·OH and BQ is the capture agent of $\cdot O_2^-$ [30-32]. As shown in Fig. **9**(a), the degradation efficiency of Rhodamine B under visible light by 2% g-C_3N_4/Bi_2S_3 was 31.6% without any capturing agent. After adding IPA, the degradation efficiency of Rhodamine B under visible light remained unchanged, indicating that there was no ·OH in this process. After adding BQ and TEOA, the degradation efficiency of Rhodamine B decreased to 15.6% and 13.5%, respectively. The results indicated that the active species in photocatalytic degradation of Rhodamine B were h^+ and $\cdot O_2^-$. In addition, electron spin resonance (ESR) measurements detected superoxide radicals using 5,5-dimethyl-1-pyrroline-n-oxide (DMPO) as the capturing agent. It can be seen from Fig. **9**(b) that there is no $\cdot O_2^-$ peak in the dark, but there is a $\cdot O_2^-$ characteristic peak at 5 min of light, and the $\cdot O_2^-$ the characteristic peak is significantly enhanced at 10 min. These results further confirmed that $\cdot O_2^-$ was one of the main active species in degrading Rhodamine B by 2% g-C_3N_4/Bi_2S_3.

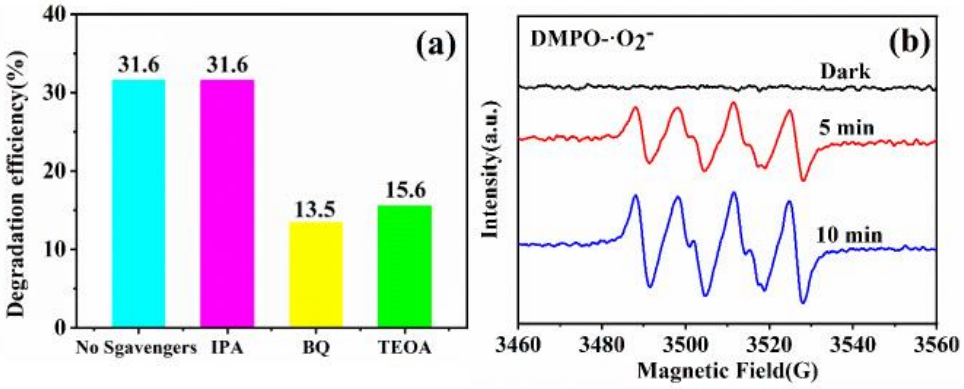

Figure 9: Photocatalytic degradation efficiency of Rhodamine B with capturing agents (a) and electron spin resonance (ESR) of DMPO-·O_2^- (b).

3.8. Mechanism

The bandgap width and flat band potential of pure Bi_2S_3 and pure g-C_3N_4 are obtained by UV-Vis diffuse reflectance spectroscopy and the Mott Schottky test. The potentials of the valence band and conduction band are calculated and are shown in Table **2**. Combined with the capturing experiment of active species, the mechanism of g-C_3N_4/Bi_2S_3 for photocatalytic reduction of Cr(VI) and degradation of organic pollutants is speculated (Fig. **10**). Under visible light, Bi_2S_3 and g-C_3N_4 are excited to produce electron-hole pairs [34, 35]. The photogenerated electron (e^-) in the conduction band (CB) of Bi_2S_3 is combined with the h^+ in the valence band (VB) of g-C_3N_4. The e^- in CB of g-C_3N_4 and the h^+ in VB of Bi_2S_3 may be involved in producing active species. The E_{VB} of Bi_2S_3 is +1.837 eV, which is less than $E_{OH^-/\cdot OH}$= +1.99 eV. Therefore, ·OH cannot be generated because OH^- cannot be oxidized by h^+ theoretically, which is confirmed by adding IPA in the capturing experiment of active species. The E_{CB} potential of g-C_3N_4 is -0.353 eV, which is lower than $E_{\cdot O_2^-/O_2}$= -0.046 eV, thus O_2 can be reduced to superoxide radical ($\cdot O_2^-$). The active species for degradation reaction are $\cdot O_2^-$ and h^+ [33]. The photogenerated electrons in CB of g-C_3N_4 also participate in reducing Cr(VI).

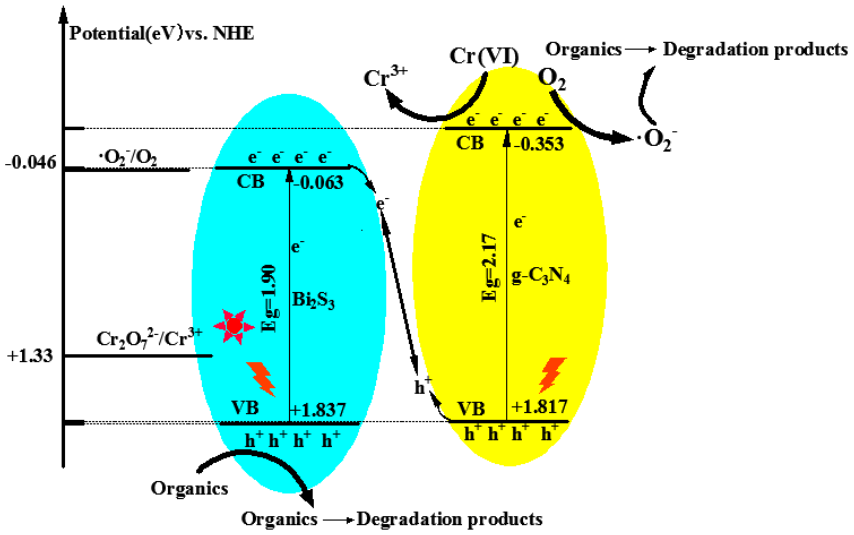

Figure 10: Photocatalytic mechanism of 2% g-C_3N_4/Bi_2S_3 for reduction of Cr(VI) and degradation of organic pollutants.

3.9. Application in Actual Pharmaceutical Wastewater

2% g-C_3N_4/Bi_2S_3 was added to the actual pharmaceutical wastewater to explore the removal of TOC and COD. As shown in Fig. (**11**), the removal rate of COD and TOC in actual pharmaceutical wastewater is 20.0% and 43.9%, indicating considerable practical application prospects of 2% g-C_3N_4/Bi_2S_3.

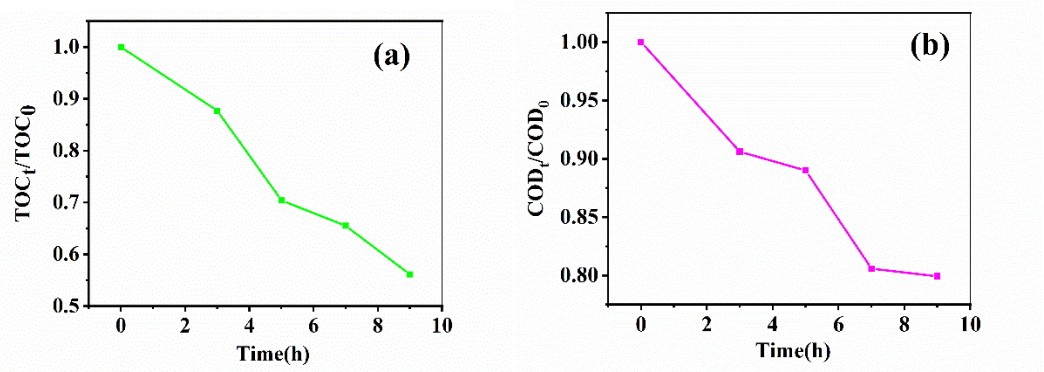

Figure 11: TOC and COD removal rate of actual pharmaceutical wastewater.

4. Conclusion

In this work, Z-scheme g-C_3N_4/Bi_2S_3 heterojunctions with intimate interface were successfully synthesized by direct growth of Bi_2S_3 on the surface of g-C_3N_4, and their photocatalytic performance was explored by reduction of Cr(VI) and degradation of Rhodamine B and TC. Among them, 2% g-C_3N_4/Bi_2S_3 has the best performance, with Cr(VI) reduction efficiency of 67.1% and 93.1% under visible light and under UV visible light, respectively. The active radical capturing experiment inferred that 2% g-C_3N_4/Bi_2S_3 is a Z-scheme heterojunction, which significantly enhances the separation rate of photogenerated electrons and holes, increasing the range of light absorption and significantly improving its photocatalytic activity. This work provides new ideas into the environmentally friendly and efficient photocatalytic reduction of Cr(VI).

Declaration of Interests

The authors have no conflicts of interest or competing financial interests to declare.

Acknowledgments

This work was financially supported by the Department of Education Fund of Jiangxi Province (GJJ210913), the Natural Science Foundation of China (51720105001, 51978324), Natural Science Foundation of Jiangxi Province (20213BCJL22053, 20192ACBL20043), Key Laboratory of Jiangxi Province for Persistent Pollutants Control and Resources Recycle (Nanchang Hangkong University) (ES202002077).

References

[1] Peng Y, Huang H, Zhang Y, Kang C, Chen S, Song L, et al. A versatile MOF-based trap for heavy metal ion capture and dispersion, Nat. Commun. 2018; 9(1): 187. https://doi.org/10.1038/s41467-017-02600-2

[2] Islam M.S, Ahmed M.K, Raknuzzaman M, Habibullah -Al- Mamun M, Islam M.K. Heavy metal pollution in surface water and sediment: A preliminary assessment of an urban river in a developing country, Ecol. Indicators 2015; 48: 282-291. https://doi.org/10.1016/j.ecolind.2014.08.016

[3] Pushkar B, Sevak P, Parab S, Nilkanth N. Chromium pollution and its bioremediation mechanisms in bacteria: A review, J. Environ. Manage. 2021; 287: 112279. https://doi.org/10.1016/j.jenvman.2021.112279

[4] Bolisetty S, Peydayesh M, Mezzenga R. Sustainable technologies for water purification from heavy metals: review and analysis, Chem. Soc. Rev. 2019; 48(2): 463-487. https://doi.org/10.1039/C8CS00493E

[5] Yuan P, Fan M, Yang D, He H, Liu D, Yuan A, et al. Montmorillonite-supported magnetite nanoparticles for the removal of hexavalent chromium [Cr(VI)] from aqueous solutions, J. Hazard. Mater. 2009; 166(2): 821-829. https://doi.org/10.1016/j.jhazmat.2008.11.083

[6] de Bittencourt M.A, Novack A.M, Scherer Filho J.A, Mazur L.P, Marinho B.A, da Silva A, et al. Application of FeCl3 and TiO2-coated algae as innovative biophotocatalysts for Cr(VI) removal from aqueous solution: A process intensification strategy, J. Cleaner Prod. 2020; 268: 122164. https://doi.org/10.1016/j.jclepro.2020.122164

[7] Kumar V, Singh V, Kim K.-H, Kwon E.E, Younis S.A. Metal-organic frameworks for photocatalytic detoxification of chromium and uranium in water, Coord. Chem. Rev. 2021; 447. https://doi.org/10.1016/j.ccr.2021.214148

[8] Cui W.R, Li F.F, Xu R.H, Zhang C.R, Chen X.R, Yan R.H, et al. Regenerable covalent organic frameworks for photo-enhanced uranium adsorption from seawater, Angew. Chem. Int. Ed. 2020; 59(40): 17684-17690. https://doi.org/10.1002/anie.202007895

[9] Liu F, Ma Z, Deng Y, Wang M, Zhou P, Liu W, et al. Tunable covalent organic frameworks with different heterocyclic nitrogen locations for efficient Cr(VI) reduction, Escherichia coli disinfection, and paracetamol degradation under visible-Light irradiation, Environ. Sci. Technol. 2021; 55: 5371-5381. https://doi.org/10.1021/acs.est.0c07857

[10] Kato H, Kudo A. Visible-light-response and photocatalytic activities of TiO2 and SrTiO3 photocatalysts codoped with antimony and chromium, J. Phys. Chem. B 2002; 106: 5029-5034. https://doi.org/10.1021/jp0255482

[11] Testa JJ, Grela M.A, Litter M.I. Heterogeneous photocatalytic reduction of chromium(VI) over TiO2 particles in the presence of oxalate: involvement of Cr(V) species, Environ. Sci. Technol. 2004; 38: 1589-1594. https://doi.org/10.1021/es0346532

[12] Repo E, Rengaraj S, Pulkka S, Castangnoli E, Suihkonen S, Sopanen M, et al. Photocatalytic degradation of dyes by CdS microspheres under near UV and blue LED radiation, Sep. Purif. Technol. 2013; 120: 206-214. https://doi.org/10.1016/j.seppur.2013.10.008

[13] Zhou R, Zhou R, Alam D, Zhang T, Li W, Xia Y, et al. Plasmacatalytic bubbles using CeO2 for organic pollutant degradation, Chem. Eng. J. 2021; 403: 126413. https://doi.org/10.1016/j.cej.2020.126413

[14] Yu J, Kudo A. Effects of structural variation on the photocatalytic performance of hydrothermally synthesized BiVO4, Adv. Funct. Mater. 2006; 16: 2163-2169. https://doi.org/10.1002/adfm.200500799

[15] Bhatkhande D.S, Pangarkar V.G, Beenackers A.A.C.M. Photocatalytic degradation for environmental applications - a review, J. Chem. Technol. Biotechnol. 2002; 77: 102-116. https://doi.org/10.1002/jctb.532

[16] Chen F, Cao Y, Jia D. Facile synthesis of Bi2S3 hierarchical nanostructure with enhanced photocatalytic activity, J. Colloid Interface Sci. 2013; 404: 110-116. https://doi.org/10.1016/j.jcis.2013.04.013

[17] Shao B, Liu X, Liu Z, Zeng G, Liang Q, Liang C, et al. A novel double Z-scheme photocatalyst Ag3PO4/Bi2S3/Bi2O3 with enhanced visible-light photocatalytic performance for antibiotic degradation, Chem. Eng. J. 2019;368: 730-745. https://doi.org/10.1016/j.cej.2019.03.013

[18] Ou J.-H, Sheu Y.-T, Tsang D.C.W, Sun Y.-J, Kao C.-M. Application of iron/aluminum bimetallic nanoparticle system for chromium-contaminated groundwater remediation, Chemosphere 2020; 256: 127158. https://doi.org/10.1016/j.chemosphere.2020.127158

[19] Sang Y, Cao X, Dai G, Wang L, Peng Y, Geng B. Facile one-pot synthesis of novel hierarchical Bi2O3/Bi2S3 nanoflower photocatalyst with intrinsic p-n junction for efficient photocatalytic removals of RhB and Cr(VI), J. Hazard. Mater. 2020; 381: 120942. https://doi.org/10.1016/j.jhazmat.2019.120942

[20] Wang S, Li X, Chen Y, Cai X, Yao H, Gao W, et al. A facile one-Pot synthesis of a two-dimensional MoS2/Bi2S3 composite theranostic nanosystem for multi-modality tumor imaging and therapy, Adv. Mater. 2015; 27: 2775-2782. https://doi.org/10.1002/adma.201500870

[21] Fu J, Yu J, Jiang C, Cheng B. g-C3N4-based heterostructured photocatalysts, Adv. Energy Mater. 2018; 8(3): 1701503. https://doi.org/10.1002/aenm.201701503

[22] Zhang X, Xie X, Wang H, Zhang J, Pan B, Xie Y. Enhanced photoresponsive ultrathin graphitic-phase C3N4 nanosheets for bioimaging, J. Am. Chem. Soc. 2013; 135: 18-21. https://doi.org/10.1021/ja308249k

[23] Ye L, Liu J, Jiang Z, Peng T, Zan L. Facets coupling of BiOBr-g-C3N4 composite photocatalyst for enhanced visible-light-driven photocatalytic activity, Appl. Catal. B: Environ. 2013; 142-143: 1-7. https://doi.org/10.1016/j.apcatb.2013.04.058

[24] Chai B, Yan J, Wang C, Ren Z, Zhu Y. Enhanced visible light photocatalytic degradation of Rhodamine B over phosphorus doped graphitic carbon nitride, Appl. Surf. Sci. 2017; 391: 376-383. https://doi.org/10.1016/j.apsusc.2016.06.180

[25] Deng Y, Tang L, Zeng G, Zhu Z, Yan M, Zhou Y, et al. Insight into highly efficient simultaneous photocatalytic removal of Cr(VI) and 2,4-diclorophenol under visible light irradiation by phosphorus doped porous ultrathin g-C3N4 nanosheets from aqueous media: Performance and reaction mechanism, Appl. Catal. B: Environ. 2017; 203: 343-354. https://doi.org/10.1016/j.apcatb.2016.10.046

[26] Lei C, Wang C, Chen W, He M, Huang B. Polyaniline@magnetic chitosan nanomaterials for highly efficient simultaneous adsorption and in-situ chemical reduction of hexavalent chromium: Removal efficacy and mechanisms, Sci. Total Environ. 2020; 733: 139316. https://doi.org/10.1016/j.scitotenv.2020.139316

[27] Zhu Y.P, Ren T.Z, Yuan Z.Y. Mesoporous phosphorus-doped g-C3N4 nanostructured flowers with superior photocatalytic hydrogen evolution performance, ACS Appl. Mater. Interf. 2015; 7: 16850-16856. https://doi.org/10.1021/acsami.5b04947

[28] Hu X, Deng F, Huang W, Zeng G, Luo X, Dionysiou D.D. The band structure control of visible-light-driven rGO/ZnS-MoS2 for excellent photocatalytic degradation performance and long-term stability, Chem. Eng. J. 2018; 350: 248-256. https://doi.org/10.1016/j.cej.2018.05.182

[29] Shi L, Yang L, Zhou W, Liu Y, Yin L, Hai X, et al. Photoassisted construction of holey defective g-C3N4 photocatalysts for efficient visible-light-driven H2O2 production, Small 2018; 14: 1703142. https://doi.org/10.1002/smll.201703142

[30] Nosaka Y, Nosaka A. Understanding hydroxyl radical (•OH) generation processes in photocatalysis, ACS Energy Lett. 2016; 1: 356-359. https://doi.org/10.1021/acsenergylett.6b00174

[31] Chu C.-Y, Huang M.H. Facet-dependent photocatalytic properties of Cu2O crystals probed by using electron, hole and radical scavengers, J. Mater. Chem. A 2017; 5: 15116-15123. https://doi.org/10.1039/C7TA03848H

[32] Nosaka Y, Nosaka A.Y. Generation and detection of reactive oxygen species in photocatalysis, Chem. Rev. 2017; 117: 11302-11336. https://doi.org/10.1021/acs.chemrev.7b00161

[33] Huang H, Tu S, Zeng C, Zhang T, Reshak A.H, Zhang Y. Macroscopic polarization enhancement promoting photo- and piezoelectric-induced charge separation and molecular oxygen activation, Angew. Chem. Int. Ed. 2017; 56: 11860-11864. https://doi.org/10.1002/anie.201706549

[34] Xu Q, Zhang L, Yu J, Wageh S, Al-Ghamdi A.A, Jaroniec M. Direct Z-scheme photocatalysts: Principles, synthesis, and applications, Mater. Today 2018; 21(10): 1042-1063. https://doi.org/10.1016/j.mattod.2018.04.008

[35] Nakada A, Kuriki R, Sekizawa K, Nishioka S, Vequizo J.J.M, Uchiyama T, et al. Effects of interfacial electron transfer in metal complex-semiconductor hybrid photocatalysts on Z-scheme CO2 reduction under visible light, ACS Catal. 8: 2018; 9744-9754. https://doi.org/10.1021/acscatal.8b03062